Passive Radar Imaging by Filling Gaps Between ISDB Digital TV Channels

Weike Feng, Jean-Michel Friedt, Grigory Cherniak, Motoyuki Sato

Passive Radar Imaging by Filling Gaps Between ISDB Digital TV Channels

Weike Feng, Jean-Michel Friedt, Grigory Cherniak, and Motoyuki Sato

Abstract—Integrated Services Digital Broadcasting-Terrestrial/Satellite (ISDB-T/S) signal, used in Japan as the digital television (TV) broadcasting standard, is exploited in this paper for passive bistatic radar two-dimensional imaging of stationary targets. A multifunctional system is developed with commercial-off-the-shelf antennas, low-noise block downconverters, and amplifiers. Several practical issues of using ISDB-T/S signals for imaging are high-lighted. Ambiguity function analysis, accurate time delay estimation, inverse filtering, and local frequency correction are carried out. Multiple TV channels are combined to improve the range resolution. In order to reduce the artifacts caused by the frequency gaps among multiple TV channels, two low-rank matrix-completion-based algorithms are proposed. Experiment results with different targets validate the performance of the designed system and the proposed algorithms.

Keywords—Integrated services digital broadcasting, low-rank matrix completion (MC), passive bistatic radar (PBR), two-dimensional (2-D) imaging.

I. Introduction

NOWADAYS, broadcasting signal, communication signal, and navigation signal are used for passive bistatic radar (PBR) applications with an increasing interest [1]–[3]. By using existing noncooperative illuminators without a dedicated radar transmitter, PBR can achieve several attractive advantages over active radar: smaller vulnerability, no need for frequency allocations, and lower cost. Various signals, such as FM radio, GSM, DAB, Digital Video Broadcasting (DVB-T/S), and Wi-Fi, have been researched to validate their performances for different applications: moving target range-Doppler mapping, synthetic aperture radar (SAR) imaging, inverse SAR (ISAR) imaging, through the wall target detection, direction finding, displacement estimation, and coherent change detection [4]–[10]. For passive radar, frequency bandwidth is one of the important considered properties of the employed signal for high-range resolution requirement. Among different noncooperative commercial signal sources, Wi-Fi signal may have the widest bandwidth: the second generation IEEE 802.11ac standard Wi-Fi signal may have a 160 MHz bandwidth [11], providing a maximal bistatic range resolution of 1.875 m. However, the low power (and thus small coverage area) of Wi-Fi communication limits it for short-range applications [12]. Digital television (TV) broadcasting signal has a narrower bandwidth than Wi-Fi but has a larger coverage capacity and a more continuous emission, while its bandwidth is also wider than some other signals (such as FM, GSM, and GPS). Therefore, digital TV signal is widely applied to airborne passive bistatic SAR imaging [13], air/coastal moving target imaging [14], [15], and ISAR imaging [16] to achieve the desired range resolution.

Currently, for terrestrial digital TV signal, four standards are mainly used in the world, including ATSC standard in USA, DVB-T standard in Europe, DTMB standard in China, and Integrated Services Digital Broadcasting-Terrestrial (ISDB-T) standard in Japan (which is the focus of this paper). For passive radar applications, DVB-T and DVB-T2 standards have been extensively researched and applied [17]–[19]. DTMB and ISDB-T standards have been employed in recent years [20]–[22]. Reference signal reconstruction, direct path interference and multipath signal suppression, ambiguity function sidelobe reduction, multiple-channel system construction, and polarization diversity investigation are the key techniques for passive radar imaging. As to passive radar using satellite digital TV signal, DVB-S and DVB-S2 signals at Ku band (typically from 10 to 12 GHz, much higher than the UHF band terrestrial signal which is typically from 400 to 800 MHz) have shown great potentials [16], [23]. Compared to terrestrial digital TV signal, satellite digital TV signal can illuminate a larger area, give a higher range resolution (the typical bandwidth of one TV channel for terrestrial signal is 6 MHz, while for satellite signal it can reach 30 MHz), and provide a clearer reference signal. However, the power density of the satellite signal at the earth surface is normally much lower than the terrestrial signal, resulting in a lower signal-to-noise ratio (SNR) and a shorter detection range. Therefore, a more complex system should be designed for passive radar imaging.

In Japan, ISDB [24] is used as the digital TV broadcasting standard. Some passive radar studies adopting ISDB-T signal for moving target detection have been conducted [20], [22], [25], while two-dimensional (2-D) imaging of stationary targets has not been well studied [26] and the ISDB-Satellite (ISDB-S)

This work was supported by JSPS Grant-in-Aid for Scientific Research (A) under Grant 26249058. The ISDB-T passive radar investigation is supported in part by the French Centre National de la Recherche Scientifique (CNRS) PEPS grant. *(Corresponding author: Weike Feng.)*

W. Feng and G. Cherniak are with the Graduate School of Environmental Studies, Tohoku University, Sendai 980-8572, Japan (e-mail: feng.weike.q4@dc.tohoku.ac.jp; grigory.chernyak.s6@dc.tohoku.ac.jp).

J.-M. Friedt is with the FEMTO-ST, Time and Frequency Department, Besançon 25030, France (e-mail: jean-michel.friedt@femto-st.fr).

M. Sato is with Center for Northeast Asian Studies, Tohoku University, Sendai 980-8576, Japan (e-mail: motoyuki.sato.b3@tohoku.ac.jp).

signal has not been considered. In this paper, we present our recent research work on PBR with ISDB-T/S signals at UHF and Ku bands for 2-D imaging of stationary targets. We have developed a PBR system based on commercial-off-the-shelf (COTS) components, including antennas, low-noise block downconverter (LNBs), and amplifiers. The data sampling is performed by a digital oscilloscope and the antennas are mounted on a rail to form a synthetic aperture for high cross-range resolution. We highlight several practical issues of using ISDB-T/S signals and these COTS components, especially the importance of the application of inverse filtering, and the frequency difference correction between different LNBs to increase the integration time for SNR improvement. With this system, we have conducted time delay estimation and 2-D range-azimuth imaging of short-range and far-range targets.

Conventionally, to increase the range resolution of PBR, multiple frequency bands of the adopted noncooperative signal are combined [27]–[30]. For example, an appropriate coherent combination of the Galileo E5a and E5b signals is conducted in [27], and multiple channels of DVB-T signals are used in [28] to generate a higher range resolution than a single DVB-T channel. However, to reduce the cross-channel interference and guarantee the high-quality signal transmission, different TV channels are separated by frequency gaps [29], which will generate artifacts in the range compression result. The high-level artifacts of strong targets may make weaker target detection difficult. Therefore, researchers have proposed some advanced signal processing algorithms to fill these gaps to suppress the artifacts. For example, a Super Spatially Variant Apodization (Super-SVA)-based method and a compressive-sensing-based method are proposed in [28] and [29], respectively. When using ISDB-T/S signal in our research, to obtain a sufficient bandwidth for high-range resolution, multiple TV channels are also combined. For ISDB-S signal, we will demonstrate the usefulness of the Super-SVA algorithm for frequency gap filling. However, for ISDB-T signal broadcast in Sendai, Japan, the frequency gaps of different channels are larger than the useful signal bandwidth, making the basic assumption of Super-SVA-based algorithm unsatisfied. For compressive-sensing-based algorithm, it is required to design a sparsifying dictionary, and the offgrid problem will degrade the performance when some sparse recovery algorithms are used [31], [32]. Specifically, for radar imaging, the sparsifying dictionary is normally a discrete Fourier transform matrix, as indicated by [31], the offgrid targets will make the sparse signal into an incompressible one. Therefore, to fill the gaps of ISDB-T signal, we propose two low-rank matrix completion (MC) [33]–[35] based methods in this paper. The proposed MC-based methods recover the frequency domain gapped signals, rather than obtain the range-compressed profiles or 2-D focused image directly by compressive-sensing-based method. After gapped signal reconstruction, Fourier transform is performed to get the range compressed profiles or 2-D focused image. Different from the compressive-sensing-based method, a sparsifying dictionary is not required.

To summarize, the key contributions of this paper are as follows:

1) A PBR system using COTS hardware is developed by using ISDB-T signal and ISDB-S signal for 2-D stationary target imaging. Several practical issues of the signal processing procedure are highlighted.
2) Two effective algorithms to fill frequency gaps among multiple TV channels based on the low-rank property of the received signal are proposed and validated.
3) Experiment results with different targets at short range and far range are presented to verify the feasibility of the designed system and the proposed algorithms.

The remainder of this paper is organized as follows. In Section II, ISDB-T and ISDB-S signals are briefly introduced. Their spectra and ambiguity functions are shown by using the real-sampled data. In Section III, the designed PBR system is presented. Then, as the first study step, time delay estimation experiment is conducted. The effectiveness of using an inverse filter and how to correct the local oscillator difference between different COTS LNBs are also presented. In Section IV, MC-based algorithms are proposed for frequency gap filling. The proposed algorithm is validated by the 1-D time delay estimation and 2-D target imaging experiments. Finally, Section V concludes this paper.

II. ISDB-T AND ISDB-S OVERVIEW

ISDB is the set of digital broadcasting standards intended to provide audio, video, and multimedia services. It has three kinds of systems, ISDB-S (Satellite), ISDB-T (Terrestrial), and ISDB-C (Cable). In this paper, we are using ISDB-T (UHF band) and ISDB-S (Ku band) for PBR studies. In this section, the basis of ISDB-T and ISDB-S is briefly introduced.

A. ISDB-T

The ISDB-T system can provide reliable high-quality video, sound, and data broadcasting for fixed and mobile receivers [36]. Three transmission modes are available for the use of a wide range of transmitting frequencies, and the transmission mode 3 with 6 MHz bandwidth and 5617 active carriers is used in Japan. Band segmented transmission-orthogonal frequency division multiplexing (BST-OFDM), which consists of a set of common basic frequency blocks called BST segments, is used as the modulation scheme for ISDB-T signal. The transmission parameters may be individually set for each segment, making for flexible channel composition. One ISDB-T symbol consists of 13 OFDM segments, and each segment occupies 6/14 MHz $= 428.6$ kHz bandwidth. When 13 active segments are used, the total useful bandwidth can be 5.57 MHz.

In Sendai (Japan), six digital TV channels are broadcast by three TV towers (Fig. 1) using horizontal polarization. The assigned frequency is from 470 to 570 MHz (Fig. 2). Four channels are emitted from the same TV tower, while the other two channels are emitted from different ones, as indicated by the rectangles in Fig. 2. In this paper, we only use three channels (473, 497, and 509 MHz), since having all emitters at the same place can simplify the bistatic geometry of the experiments and their frequency gaps are not too large to handle with. Combining different TV channels from different TV towers for target locating application is under consideration. For PBR, range resolution is

Fig. 1. Three TV towers located 3.3 km from our laboratory broadcast in the Sendai (Japan) area. Background map: Google Maps.

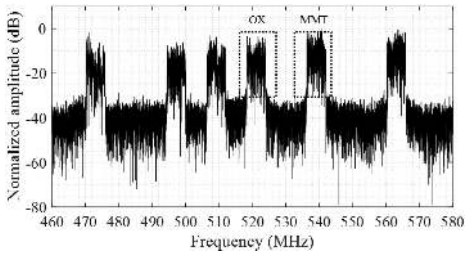

Fig. 2. Spectrum of ISDB-T signal in Sendai. OX and MMT are broadcast by different TV towers from the other four channels.

defined as

$$\Delta r = c/[2B\cos(\beta/2)] \tag{1}$$

where c is the speed of light, B is the signal bandwidth, and β is the bistatic angle. As we are using three ISDB-T TV channels, the total bandwidth can reach about 42 MHz, giving a maximal range resolution $\Delta r_{\max} = 3.57$ m when $\beta = 0$.

Besides the range resolution, another property of ISDB-T signal that should be considered is its ambiguity function, as defined by (2), which describes not only its ambiguity but also its clutter suppression performance.

$$\chi(\tau, f_d) = \int_0^{T_{\text{int}}} s_{\text{ref}}(t) s_{\text{ref}}^*(t-\tau) e^{-j2\pi f_d t} dt \tag{2}$$

where $s_{\text{ref}}(t)$ is the received reference signal, $(\cdot)^*$ denotes the complex conjugate, $\chi(\tau, f_d)$ is the range-Doppler map of targets, τ and f_d are the expected time delay and Doppler frequency of the target, and T_{int} is the integration time. Since we are focusing on stationary target imaging, we will use $f_d = 0$ in this paper. Fig. 3 shows the ambiguity function of the real-sampled ISDB-T signal with an integration time of 10 μs. It can be seen that, although the range resolution matches the calculation of (1), the signal structure and frequency gaps among three channels cause high-level artifacts, which should be suppressed for a better range compression.

B. ISDB-S

Japan began digital broadcasting using a communication satellite (CS) on the geostationary orbit of 128° east longitude (CS 128 °E) with DVB-S standard. Now, digital broadcasting with broadcasting satellite (BS) and CS on the geostationary

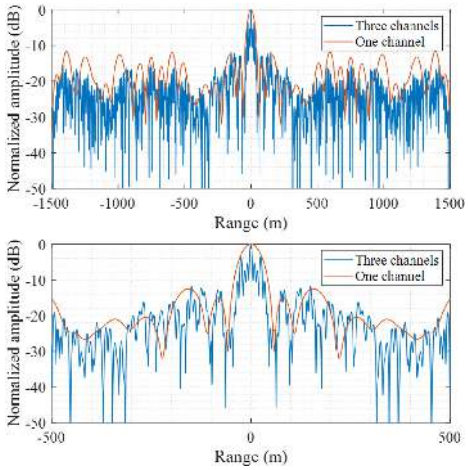

Fig. 3. Ambiguity function of three ISDB-T TV channels with an integration time of 10 μs. The bottom subfigure is the zoomed version of top subfigure.

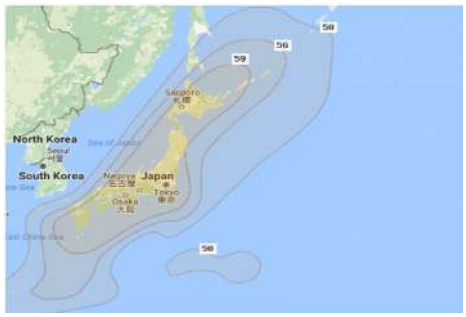

Fig. 4. Covered area of CS satellite with different Equivalent Isotropically Radiated Powers (EIRPs), provided by LyngSat website.

orbit of 110° east longitude (BS/CS 110 °E) is using ISDB-S standard [37]. Compared with DVB-S, ISDB-S adopts the Trellis coded 8-phase shift keying modulation, enabling the broadcasting of two high-quality programs with one transponder.

The frequency transfer function of ISDB-S is a raised cosine roll-off filter with a roll-off factor of 0.35. The data rate is typically 52.2 Mbit/s in one transmission channel that has a frequency bandwidth of 34.5 MHz. As to the transmitted waves, both BS and CS use a right-hand circular polarization. However, from the end of 2018, left-hand circular polarization will also be applied by BS and CS for higher quality TV program transmission. Compared with broadcasting with ISDB-T, which can only provide services for a local region, broadcasting with ISDB-S can cover the whole country of Japan, as shown in Fig. 4. For the operating frequency, BS satellite is using 11.7 to 12.2 GHz band and CS satellite is using 12.2 to 12.75 GHz band. With a 10.678 GHz local oscillation frequency of the LNB, the spectrum of real-sampled BS and CS signals is shown in Fig. 5. As we can see, BS and CS bands all have about 475.5 MHz bandwidth. However, channel 7 and 17 in BS band are missing, since they are used for 4K transmission test. Therefore, in this paper, we will only adopt CS signal for PBR studies.

For ISDB-S CS signal, the frequency bandwidth can reach 474.5 MHz by combining 12 channels, resulting in a maximal range resolution 0.32 m, much higher than the ISDB-T signal. The ambiguity function of CS signal is shown in Fig. 6, from

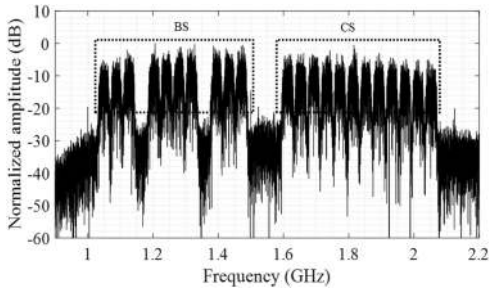

Fig. 5. Spectrum of ISDB-S signal in Japan. BS and CS are broadcast by different satellites. The local oscillation frequency of LNB is 10.678 GHz.

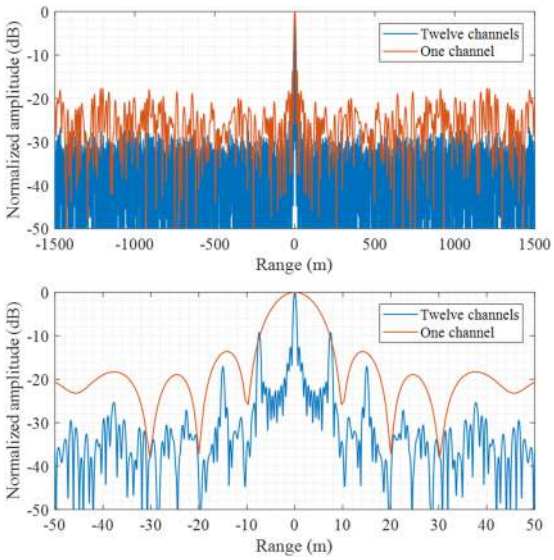

Fig. 6. Ambiguity function of CS ISDB-S signal with an integration time of 10 μs. The bottom subfigure is the zoomed version of top subfigure.

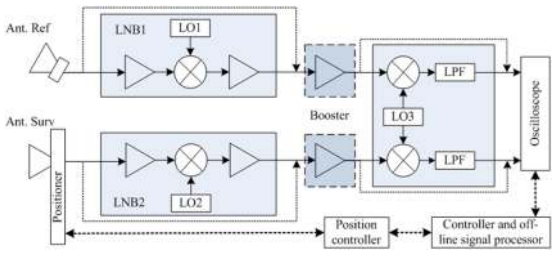

Fig. 7. Block diagram of the designed PBR system.

which we can learn that high-level artifacts around the zero time delay are produced by the signal structure and frequency gaps. Because the received ISDB-S signal has much less multipath influence than the ISDB-T signal, it can also be seen that Fig. 6 has a higher SNR than Fig. 3.

III. Designed PBR System

A. System Architecture

For PBR, two parallel receiving channels (reference and surveillance) are inherently needed. Fig. 7 presents the block diagram of the developed PBR system using ISDB-T/S signals.

In our study, two 18-element Yagi-Uda antennas (reference and surveillance) will be used for ISDB-T-based experiments, and two 45 cm parabolic antennas will be used for ISDB-S-based experiments. We note that, for target imaging, only the feed horn of the surveillance parabolic antenna is used to increase the beamwidth, which will be presented in Section IV. The LNBs with a local frequency of 10.678 GHz (working frequency 11.71 to 12.75 GHz, output frequency 1032 to 2072 MHz, right-hand circular polarization, gain 53 dB, and noise figure 0.45 dB) are not necessary for the ISDB-T setup, and since two LNBs have different local oscillators (LO1 and LO2), phase drift occurs, which will reduce the coherence of two receiving channels and thus should be corrected.

Two COTS BS/110°CS/UHF boosters are used to further amplify the received signal. Their working frequency is from 10 to 2600 MHz, the gain for UHF is from 30 to 36 dB adjustable, and the gain for BS/CS is from 26 to 34 dB adjustable. After booster, the signal flow will pass a second downconverter (including a common local signal generator, two frequency mixers, and two low-pass filters) to lighten the sampling burden. However, we note that, in this paper, since we are using a digital storage oscilloscope (maximum sampling frequency 20 GHz, memory 16 MB, and four channels can be used at the same time) to sample, save and transfer the dataset, this second downconverter is also not necessary currently but will be used in the next step when an Ettus Research universal software radio peripheral is ready. Finally, the sampled data of the oscilloscope will be transferred to a local PC, which is also used to control the programmable positioner to scan the antennas with a fix step in horizontal and/or vertical directions, for offline signal processing, including phase drift correction, inverse filtering, frequency gap filling, range compression, and azimuth focusing.

B. Time Delay Estimation

As the first research stage, we test the capability of the designed PBR system using ISDB-T/S as illumination sources for passive radar imaging by conducting time delay estimation experiments. In these experiments, reference and surveillance antennas are both facing toward the TV tower or CS satellite (35.3° elevation angle and 224° azimuth angle). The reference antenna is stationary, while the surveillance antenna is moved along a base line, as shown in Fig. 8.

Without considering the multipath echoes, the signal received by the reference antenna can be expressed as

$$s_{\text{ref}}(t) = A_{\text{ref}} s_0(t - t_{\text{ref}}) + n_{\text{ref}}(t) \tag{3}$$

where $s_0(t)$ is the transmitted signal, A_{ref} is the complex amplitude, t_{ref} denotes the transmission time from the TV tower/satellite to the reference antenna, and $n_{\text{ref}}(t)$ denotes additive noise. Similarly, the surveillance signal is given by

$$s_{\text{sur}}(t) = A_{\text{sur}} s_0(t - t_{\text{sur}}) + n_{\text{sur}}(t) \tag{4}$$

where A_{sur} is the amplitude of the received signal with time delay t_{sur} and $n_{\text{sur}}(t)$ is additive noise. The classical way to estimate the time delay between two antennas, i.e., to get the range compression result, is to calculate their cross-correlation

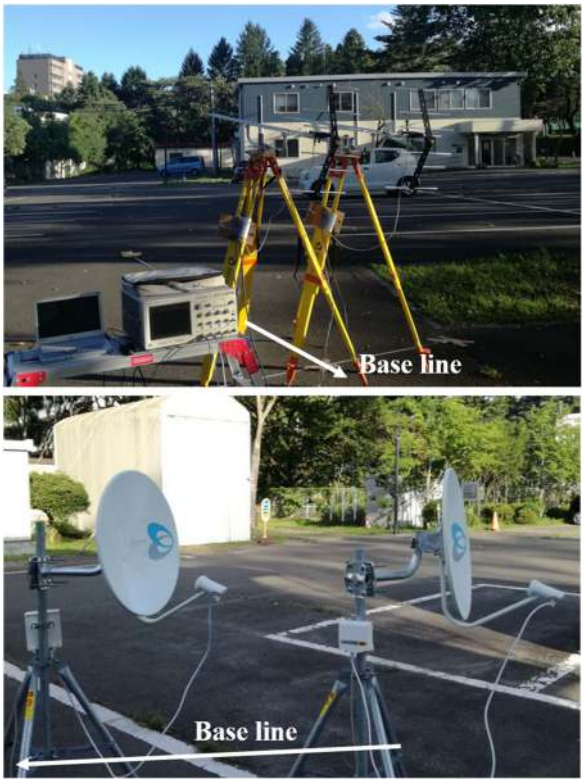

Fig. 8. Time delay estimation experiments with (top) ISDB-T signal and (bottom) ISDB-S signal.

function, expressed as

$$\chi(\tau) = \int_0^{T_{\text{int}}} s_{\text{sur}}(t) s_{\text{ref}}^*(t-\tau) dt. \tag{5}$$

Cross-correlation processing can be conducted by implementing fast Fourier transform, resulting in

$$\boldsymbol{\chi} = \boldsymbol{\Phi}^H \boldsymbol{s}(\boldsymbol{f}) = \boldsymbol{\Phi}^H [\boldsymbol{s}_{\text{sur}}(\boldsymbol{f}) \odot \boldsymbol{s}_{\text{ref}}(\boldsymbol{f})^*] \tag{6}$$

where $\boldsymbol{\Phi}$ is Fourier transform matrix, $\odot$ denotes the elementwise multiplication, $(\cdot)^H$ denotes the conjugate transpose, $\boldsymbol{f}$ is the frequency vector, and $\boldsymbol{s}_{\text{ref}}(\boldsymbol{f})$ and $\boldsymbol{s}_{\text{sur}}(\boldsymbol{f})$ are the frequency domain signals of reference and surveillance channels.

Time delay estimation results obtained by (6) are shown in Fig. 9 for several different distances between two antennas. It is observed that, although the time delay can be accurately estimated, due to the signal structure of the ISDB-T/S signals and the frequency gaps between used channels, the time delay estimation results have high-level artifacts (visible at about 25 m for the ISDB-T signal, 7.5 and 15 m for the ISDB-S signal). When applied to 2-D target imaging, the high-level artifacts of strong targets will make the weaker targets undetectable. Therefore, these artifacts should be suppressed. Besides, it can also be noticed that, compared with ISDB-S results, ISDB-T estimation has more artifacts, which is caused by the multipath signals in the ISDB-T received signal, while the ISDB-S signal will be much cleaner, as mentioned previously in Section II.

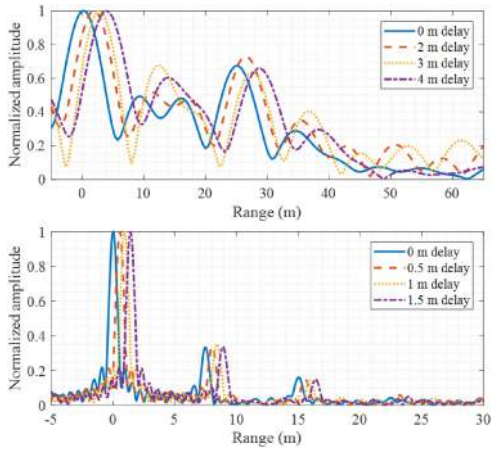

Fig. 9. Estimated time delays between two antennas. Top: ISDB-T with four different distances (0, 2, 3, and 4 m). Bottom: ISDB-S with four different distances (0, 0.5, 1, and 1.5 m). Integration time is 10 μs.

C. Inverse Filter and Local Frequency Correction

Since ISDB-T/S is used for communication purpose, their waveforms are not designed for radar application. Therefore, due to spectrum properties, pilot signals, and guard intervals, high-level artifacts will be produced by cross-correlation processing, as shown in the previous subsection. These artifacts cannot be suppressed by the classical amplitude windowing methods. A simple method to solve this problem is to use an inverse filter to avoid the influence of the signal structure of ISDB-T/S. Considering the ideal case, where the frequency domain signals $\boldsymbol{s}_{\text{ref}}(\boldsymbol{f})$ and $\boldsymbol{s}_{\text{sur}}(\boldsymbol{f})$ statisfy (assuming $\alpha = A_{\text{surv}}/A_{\text{ref}}$)

$$\boldsymbol{s}_{\text{sur}}(\boldsymbol{f}) = \alpha e^{-j2\pi \boldsymbol{f}(t_{\text{sur}} - t_{\text{ref}})} \odot \boldsymbol{s}_{\text{ref}}(\boldsymbol{f}). \tag{7}$$

Equation (6) can be rewritten as

$$\boldsymbol{\chi} = \boldsymbol{\Phi}^H \boldsymbol{s}(\boldsymbol{f}) = \boldsymbol{\Phi}^H \left[\alpha e^{-j2\pi \boldsymbol{f}(t_{\text{sur}} - t_{\text{ref}})} \odot |\boldsymbol{s}_{\text{ref}}(\boldsymbol{f})|^2\right]. \tag{8}$$

Thus, an inverse filter can be constructed as follows to reduce the influence of the signal properties of ISDB-T/S:

$$\boldsymbol{\chi}' = \boldsymbol{\Phi}^H s'(\boldsymbol{f}) = \boldsymbol{\Phi}^H \left[\boldsymbol{s}_{\text{sur}}(\boldsymbol{f}) \odot \boldsymbol{s}_{\text{ref}}(\boldsymbol{f})^* / |\boldsymbol{s}_{\text{ref}}(\boldsymbol{f})|^2\right]. \tag{9}$$

With same datasets for Fig. 9, time delay estimation results obtained by using an inverse filter are shown in Fig. 10. It can be observed that the artifacts can be effectively mitigated by the inverse filter, especially in the ISDB-S-based cases. For the ISDB-T-based experiments, the usefulness of inverse filter is not so obvious, which is caused by the larger frequency gaps and the stronger multipath influences. We will propose an MC-based frequency gap filling method to further improve its quality in the next section.

Although time delay estimation results of ISDB-S signal seem promising as shown in Figs. 9 and 10, in the real case, the SNR of signals reflected by targets will be much lower than the direct signal. To increase the SNR, a natural idea is to increase the integration time. However, two COTS LNBs have different local oscillators, resulting in slightly different local frequencies for reference and surveillance channels. Then, if a longer integration time is used, the SNR will not be increased but be reduced because two channels are no longer coherent, as shown in Fig. 11

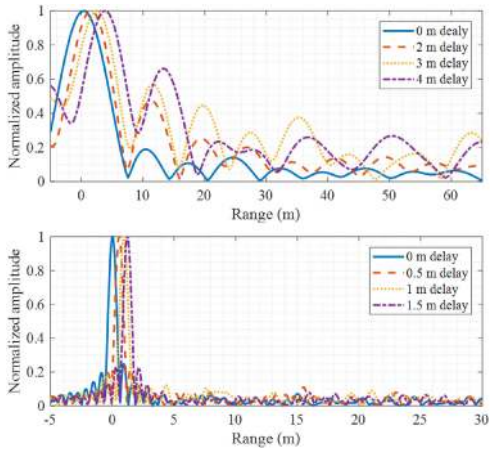

Fig. 10. Estimated time delays between two antennas using an inverse filter. Top: ISDB-T signal. Bottom: ISDB-S signal. Integration time is 10 μs.

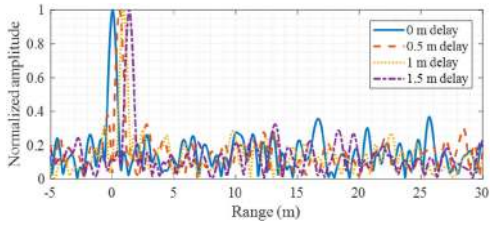

Fig. 11. Estimated delays of ISDB-S signal with a 100 μs integration time.

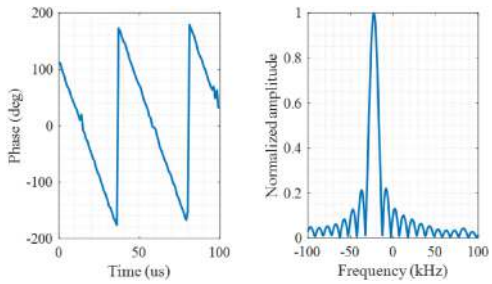

Fig. 12. (Left) phase drift caused by the frequency difference of two LNBs and (Right) frequency difference estimated by Fourier transform.

with a 100 μs integration time in comparison with Fig. 10 with a 10 μs integration time.

To solve this problem, coarse correction of the phase drift can be conducted by the following steps.

1) Divide the full-length ($T_{\text{int}} = UT$) signal to U short-length (T) subsets, within which the phase difference can be assumed to be constant, i.e., $f_0 t$, where $t = [0, T, \ldots, (U-1)T]$ and f_0 is the local oscillation frequency difference between two LNBs.
2) Do cross correlation between two colocated reference and surveillance antennas and obtain the phase of peak in each subset, which gives $e^{-j2\pi f_0 t}$.
3) Finally, do Fourier transform of the peak phases, providing us with f_0.

The phase drift and estimated frequency difference are shown in Fig. 12. The estimated frequency difference is about 22.48 kHz, within the range provided by the manual from the LNB manufacturer. We note that a tradeoff should be made to

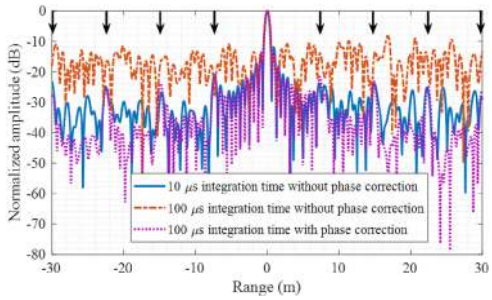

Fig. 13. Estimated time delay between two colocated antennas using ISDB-S signal with different integration time in dB scale.

balance the SNR of each subset and the unambiguous frequency determined by T. If T is too small, the phase of peak in each subset cannot be estimated accurately. If T is too big, the assumption of constant phase in each subset will not be satisfied and the unambiguous frequency will be too small to estimate the real frequency difference. In this paper, we set $T = 1$ μs, giving a maximal unambiguous frequency 500 kHz, which works properly, as shown in Fig. 13. We should also notice from Fig. 13 that, because of the frequency gaps among ISDB-S channels, high-level artifacts appear, as indicated by the arrows in Fig. 13. When using a 10 μs integration time, these artifacts are not obvious but hidden by the noise because of the lower SNR.

IV. Frequency Gap Filling

In this section, we focus on filling the frequency gaps among different ISDB-T/S channels. The problem of filling spectral gaps has been addressed in the literature. For example, autoregressive-based gap filling method is used in [38] and Super-SVA-based method is applied in [39], [40]. For passive radar imaging with multiple DVB-T channels, [28] and [41] have shown the effectiveness of Super-SVA, where the spectral gaps are small compared with the useful signal bandwidth. Therefore, in this paper, for ISDB-S-based PBR, which also enjoys small spectral gaps, as we can see in Fig. 5, Super-SVA will be applied. In Section A, the principle of Super-SVA will be briefly reviewed and then be used for ISDB-S gaps filling for 1-D range compression.

For three ISDB-T channels used in our study, their spectral gaps are larger than the useful bandwidth, as we can see in Fig. 2. Super-SVA-based method is not effective in this case [29]. For DVB-T-based ISAR imaging, [29] has proposed a compressive-sensing-based method to obtain the focused ISAR image, and an inverse processing is conducted to estimate the complete data in order to compare the result with conventional-matched-filtering-based method. However, for this method, the gapped signal reconstruction quality is affected by the offgrid problem that is introduced by the predefined sparsifying dictionary (discrete Fourier transform matrix) when some specific sparse recovery algorithms are adopted [31]. Therefore, in Section B, by exploiting the low-rank property of the received signal, we will propose two MC-based gap filling methods without designing a sparsifying dictionary, for both 1-D range compression and 2-D SAR imaging.

A. Super-SVA for ISDB-S

Super-SVA is based on SVA [42], which is an algorithm that can effectively suppress the sidelobes of Fourier transform without broadening the mainlobe. Specifically, SVA is a nonlinear operator based on the following "cosine on pedestal" weighting function in frequency domain

$$W_0(m) = 1 + 2\beta\cos(2\pi m/M), 0 \le \beta \le 0.5 \tag{10}$$

where $m = 1, 2, \ldots, M$ is the frequency index and M is the number of frequencies in each ISDB-S channel (same as the number of range bins of the range compression result of each ISDB-S channel). With this weighting function, the range compression for the nth ISDB-S channel ($n = 1, 2, \ldots, N$ and $N = 12$) can be obtained by

$$\boldsymbol{\chi}^n_{\text{SVA}} = \boldsymbol{\Phi}^H_{\boldsymbol{n}}[\boldsymbol{s}'_{\boldsymbol{n}}(\boldsymbol{f}) \odot \boldsymbol{W}(\boldsymbol{f})] \tag{11}$$

where $\boldsymbol{s_n}'(\boldsymbol{f})$ is the frequency domain signal of the nth ISDB-S channel obtained by Fourier transform and inverse filtering. Equation (11) results in the following time domain signal:

$$\boldsymbol{\chi}^n_{\text{SVA}}(m) = \beta(m)\boldsymbol{\chi}'_{\boldsymbol{n}}(m-1) + \boldsymbol{\chi}'_{\boldsymbol{n}}(m) + \beta(m)\boldsymbol{\chi}'_{\boldsymbol{n}}(m+1) \tag{12}$$

where $\boldsymbol{\chi}'_{\boldsymbol{n}}$ is the range compression result of the nth ISDB-S channel. Without the constraint in (10), the optimal $\beta(m)$ is given by

$$\beta_{\text{opt}}(m) = \text{Re}\left[\frac{-\boldsymbol{\chi}'_n(m)}{\boldsymbol{\chi}'_n(m-1) + \boldsymbol{\chi}'_n(m+1)}\right]. \tag{13}$$

Letting $\beta(m)$ satisfy $0 \le \beta(m) \le 0.5$, we can get the following range compression result:

$$\boldsymbol{\chi}^n_{\text{SVA}}(m) = \begin{cases} \boldsymbol{\chi}'_n(m), & \beta_{\text{opt}}(m) < 0 \\ \boldsymbol{\chi}'_n(m) + [\boldsymbol{\chi}'_n(m-1) + \boldsymbol{\chi}'_n(m+1)]/2, & \beta(m) > 0.5 \\ \boldsymbol{\chi}'_n(m) + \beta_{\text{opt}}(m)[\boldsymbol{\chi}'_n(m-1) + \boldsymbol{\chi}'_n(m+1)], & \text{otherwise} \end{cases}. \tag{14}$$

With SVA filter, the mainlobe can be maintained, while the sidelobes are suppressed. Based on this property, Super-SVA extrapolates the signal spectrum by the following steps.

1) Perform Fourier transform of $\boldsymbol{\chi}^n_{\text{SVA}}$, giving us $\boldsymbol{s}^n_{\text{SVA}}(\boldsymbol{f}) = \boldsymbol{\Phi}_n\boldsymbol{\chi}^n_{\text{SVA}}$, which is no longer a band-limited signal, where $\boldsymbol{\Phi}_n$ is the Fourier transform matrix for the nth ISDB-S channel.
2) By applying an inverse weight $\boldsymbol{W}_{\text{inv}}(\boldsymbol{f})$, which is the inverse Fourier transform of the mainlobe of a Sinc function, obtain the frequency signal $\boldsymbol{s}^n_{\text{Super-SVA}}(\boldsymbol{f}) = \boldsymbol{s}^n_{\text{SVA}}(\boldsymbol{f})/\boldsymbol{W}_{\text{inv}}(\boldsymbol{f})$, which has a wider bandwidth than $\boldsymbol{s_n}'(\boldsymbol{f})$. Of course, its bandwidth cannot be infinite because normally it should be truncated to avoid singularities during the inverse processing. In our case, we will only expand the spectrum to fill the gap between two adjacent ISDB-S channels.
3) Replace the center portion of the extrapolated signal $\boldsymbol{s}^n_{\text{Super-SVA}}(\boldsymbol{f})$ with the original signal $\boldsymbol{s_n}'(\boldsymbol{f})$.

According to the principle of Super-SVA, for each ISDB-S channel, the gapped signal can be reconstructed. Since two adjacent channels have the same gapped frequencies, a simple average will be conducted to make the estimation more accurate. Fig. 14 shows the time delay estimation results with and without filling frequency gaps by Super-SVA. It can be learned that, since the spectrum becomes more continuous, high-level artifacts are effectively suppressed.

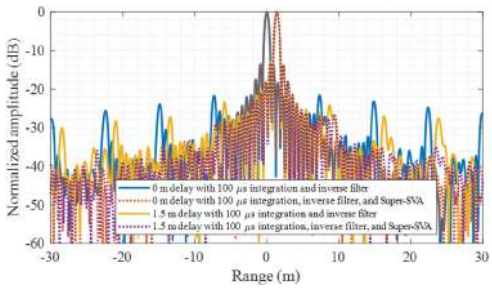

Fig. 14. Estimated time delays with and without using Super-SVA.

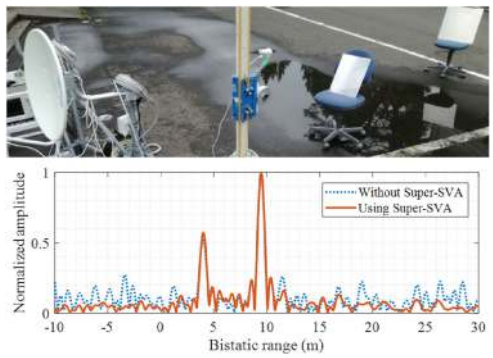

Fig. 15. Detection of two metallic plates with ISDB-S signal, the feedhorn of the surveillance antenna is used in this case to increase the beamwidth.

Fig. 16. Detection of three metallic plates with the surveillance antenna sledded on the positioner with a 5 mm step.

Then, instead of facing both antennas to the CS satellite, the feedhorn of the surveillance antenna is used to detect two metallic plates, as shown in the top of Fig. 15. The detection result is shown in the bottom of Fig. 15. As we can see, two metallic plates can be well detected by the designed ISDB-S-based PBR system. Furthermore, by using Super-SVA to reconstruct the spectral gapped signal, the artifacts of the detection result are effectively suppressed.

Furthermore, the surveillance antenna is sled on the positioner to detect three metallic plates located at different positions, as shown in Fig. 16. The moving step is 5 mm and the total sledding length is 1.4 m. We note that, although the frequency drift between two COTS LNBs can be corrected by the proposed method in the previous section, their initial phases at different antenna positions cannot be well synchronized. In such a case,

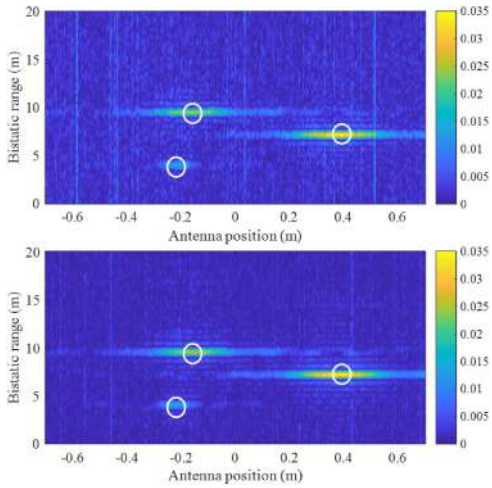

Fig. 17. 2-D imaging of three metallic plates with ISDB-S signal. Top: without using Super-SVA. Bottom: using Super-SVA to fill frequency gaps.

synthetic aperture processing cannot be carried out to increase the cross-range resolution. However, as shown in the top of Fig. 17, because of the narrow beamwidth of the surveillance antenna and the reflection properties of the metallic plate (which depends on the incident angle of the ISDB-S signal), the range and cross range of these three metallic plates can be well determined without synthetic aperture processing but with only range compression at each antenna position. To further improve the imaging quality, Super-SVA is applied to fill the frequency gaps to suppress the artifacts, whose result is shown in the bottom of Fig. 17. It is clear that, with the reconstructed signal, the range compression result becomes better. But, it should be noted that, by synchronizing the phase of two LNBs and then using the back projection (BP) algorithm [43], [44] to do the azimuth focusing, the resolution of the imaging result in the azimuth direction can be further improved, which is still under study.

B. MC for ISDB-T

MC algorithm is proposed to recover a low-rank matrix $\boldsymbol{X}$ from its small set of corrupted entries. Define the observation operation $\boldsymbol{Y} = P_{\Omega}(\boldsymbol{X})$ as

$$\boldsymbol{Y}_{i,j} = \begin{cases} \boldsymbol{X}_{i,j} + \boldsymbol{N}_{i,j}, & (i,j) \in \Omega \\ 0, & \text{otherwise} \end{cases} \tag{15}$$

where $\boldsymbol{\Omega}$ is the set of indices of the partially observed elements and $\boldsymbol{N}$ is the observation noise matrix.

When $\boldsymbol{X}$ is low rank and some conditions are satisfied [34], the unobserved elements of $\boldsymbol{X}$ can be estimated by solving the following problem:

$$\min \operatorname{rank}(\boldsymbol{X}) \quad \text{s.t. } \|P_{\Omega}(\boldsymbol{Y} - \boldsymbol{X})\|_F \leq \varepsilon \tag{16}$$

where $||\cdot||_F$ denotes the Frobenius norm of a matrix and ε is the noise level. Since (16) is NP-hard, a modified optimization problem, which can give the same solution as (16) in some conditions [34], is given by

$$\min \|\boldsymbol{X}\|_* \quad \text{s.t. } \|P_{\Omega}(\boldsymbol{Y} - \boldsymbol{X})\|_F \leq \varepsilon \tag{17}$$

where $||\cdot||_*$ denotes the nuclear norm of a matrix, which is the sum of its singular values. The nuclear norm minimization is a convex function, which can be easily solved by many state-of-the-art algorithms [35]. In this paper, inexact augmented Lagrange multiplier (IALM) algorithm [45] is used for its reconstruction accuracy and large-scale data processing efficiency. For IALM algorithm, there are three inputs: the observed data with entries corresponding to frequency gaps set to zero, the tolerance for stopping tol, and the maximum iteration number maxIter. For all experiments, we set tol $= 10^{-2}$ and maxIter $= 100$ empirically.

Compared to compressive sensing method, MC can be used to reconstruct the missing data without designing an accurate sparsifying dictionary, and thus has been used in many radar applications, such as change detection, ISAR, and tomography SAR [46]–[48]. We introduce MC algorithm to ISDB-T-based PBR to recover the signal corresponding to the gapped frequencies. Consider the frequency domain signal vector $\boldsymbol{s}'(\boldsymbol{f})$ in (9), given by

$$\begin{aligned} \boldsymbol{s}'(\boldsymbol{f}) &= \boldsymbol{s}_{\text{sur}}(\boldsymbol{f}) \odot \boldsymbol{s}_{\text{ref}}(\boldsymbol{f})^* / |\boldsymbol{s}_{\text{ref}}(\boldsymbol{f})|^2 \\ &= \alpha \exp\left(-j2\pi \boldsymbol{f} \tau_0\right) + \boldsymbol{n} \end{aligned} \tag{18}$$

and rearrange it as a matrix

$$\boldsymbol{S} = \alpha [\mathrm{e}^{-j2\pi f_1 \tau_0}, \ldots, \mathrm{e}^{-j2\pi f_P \tau_0}]^{\mathrm{T}} [1, \ldots, \mathrm{e}^{-j2\pi f_{(Q-1)P} \tau_0}] + \boldsymbol{N} \tag{19}$$

where $\tau_0 = t_{\text{sur}} - t_{\text{ref}}$ is the time delay between reference and surveillance channels, the number of frequencies of $\boldsymbol{f}$ is O, and $QP = O$.

It can be learned that $\boldsymbol{S}$ is a noise corrupted rank-one matrix, while MC theory cannot directly be applied to recover the missing data of $\boldsymbol{S}$, which has fully missing columns/rows caused by the continuous missing frequencies. However, by rearranging the original signal matrix $\boldsymbol{S}$ as a matrix $\boldsymbol{S}^0_{\text{hankel}}$ with a Hankel structure [49], [50], MC theory can be applied to estimate the gapped frequency components, expressed as

$$\begin{aligned} &\min \|\boldsymbol{S}_{\text{hankel}}\|_* \\ &\text{s.t. } \left\|P_{\Omega}^{\text{hankel}}(\boldsymbol{S}_{\text{hankel}} - \boldsymbol{S}^0_{\text{hankel}})\right\|_F \leq \varepsilon_{\text{hankel}} \end{aligned} \tag{20}$$

where $\varepsilon_{\text{hankel}}$ denotes noise level, $\boldsymbol{S}_{\text{hankel}}$ is the estimated complete Hankel structured signal matrix, and $P_{\Omega}^{\text{hankel}}$ indicates the positions of the frequencies within three useful ISDB-T TV channels in a structured Hankel form. After obtaining $\boldsymbol{S}_{\text{hankel}}$, matrix $\boldsymbol{S}$ and gap filled signal vector $\boldsymbol{s}'_{\text{MC}}(\boldsymbol{f})$ can be easily reconstructed. Then, the range compression can be obtained by Fourier transform as

$$\boldsymbol{\chi}_{\text{MC}} = \boldsymbol{\Phi}^H \boldsymbol{s}'_{\text{MC}}(\boldsymbol{f}). \tag{21}$$

We note that, in the formulation of the proposed method, in order to make it correspond to the time delay estimation experiments, it is assumed that there is only one time delay between two channels. However, in real case where there are

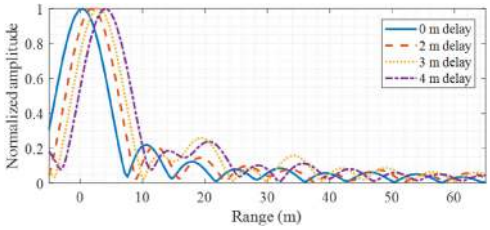

Fig. 18. Estimated time delays between two antennas with gapped signal reconstructed by the proposed MC-based method.

multiple targets, (19) should be changed to

$$\boldsymbol{S} = \sum_{i=1}^{I} \alpha_i [\mathrm{e}^{-j2\pi f_1 \tau_i}, \ldots, \mathrm{e}^{-j2\pi f_P \tau_i}]^{\mathrm{T}} [1, \ldots, \mathrm{e}^{-j2\pi f_{(Q-1)P} \tau_i}] + \boldsymbol{N} = \sum_{i=1}^{I} \alpha_i \boldsymbol{S}_i + \boldsymbol{N}. \quad (22)$$

Consequently, the rank of $\boldsymbol{S}$ is limited by

$$\mathrm{rank}\,(\boldsymbol{S}) = \mathrm{rank}\left(\sum_{i=1}^{I} \alpha_i \boldsymbol{S}_i\right) \leq \sum_{i=1}^{I} \mathrm{rank}(\boldsymbol{S}_i) = I \quad (23)$$

where α_i is the amplitude of the ith target, $i = 1, 2, \ldots, I$, and I is the target number. Therefore, if the number of targets is less than P and Q, $\boldsymbol{S}$ still has the low-rank property. And thus, the frequency gaps can still be filled by (20).

With the MC-based frequency gap filling method, the estimated time delays are shown in Fig. 18, where the high-level artifacts have been effectively mitigated compared with the results shown in the top of Fig. 10.

Besides, as shown in (17) and (20), by solving the MC problem with an iteration stopping criterion determined by the noise level, denoising can be achieved because only the low-rank components of the received signal are reconstructed. Therefore, the MC-based method cannot only fill the spectral gaps but also increase the SNR, as we can see from Fig. 18. More details about the denoising capability of MC can be found in [34]. To further validate the proposed MC-based spectral gap filling method for ISDB-T signal, a high building is used as the target, which is indicated by the rectangle in the top of Fig. 19, where the designed PBR system is located at the position indicated by the arrow, and the detection result is shown in the bottom of Fig. 19. It can be seen that, the building can be effectively detected, with a distance of about 175 m, matching the measurement on georeferenced aerial pictures. After reconstructing the gapped signal, the high-level artifacts can be well suppressed.

Actually, the proposed MC-based gap filling method can also be used for ISDB-S signal. Using the same dataset as Fig. 15, the detection results of two metallic plates are shown in Fig. 20. Because of the huge memory usage and computing time, in this case, we use a 10 μs integration time in comparison with Fig. 15 with a 100 μs integration time. It can be seen from Fig. 20 that, due to its denoising capability, the proposed MC-based method can achieve a better result than the Super-SVA-based method. However, considering the computational efficiency, in practice,

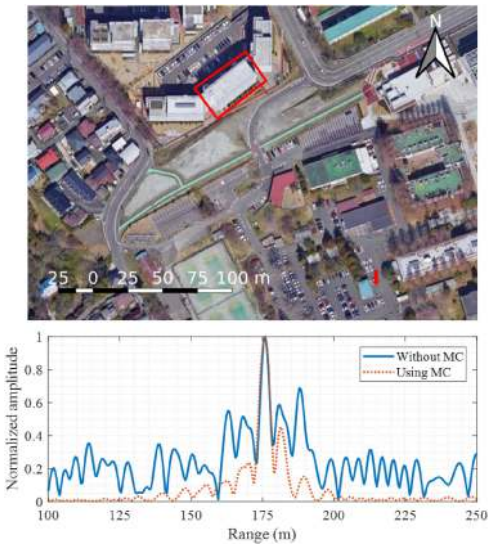

Fig. 19. Building detection results with and without MC-based gap filling.

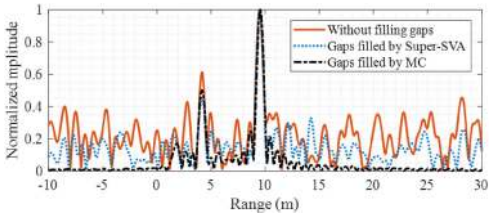

Fig. 20. Detection of two metallic plates with ISDB-S signal by different gap filling methods with an integration time of 10 μs.

Fig. 21. Reference and surveillance antennas are both mounted on the rail.

the Super-SVA-based method should be the first selection for ISDB-S signal.

Based on above studies, passive SAR experiments with ISDB-T signal were conducted for 2-D stationary target imaging. In this case, the same building is used as the target and two antennas are both fixed at the positioner to simplify the imaging geometry, as shown in Fig. 21. The antenna moving step is 10 cm and the synthetic aperture length is 2 m. At each antenna position, the data sampling frequency is 2 GHz and the integration time is 10 μs.

At the lth antenna position $(x_l, 0)$, the frequency domain signal can be expressed as

$$\begin{aligned} \boldsymbol{s}_l{}'(\boldsymbol{f}) &= \boldsymbol{s}^l_{\mathrm{sur}}(\boldsymbol{f}) \odot \boldsymbol{s}^l_{\mathrm{ref}}(\boldsymbol{f})^* / |\boldsymbol{s}^l_{\mathrm{ref}}(\boldsymbol{f})|^2 \\ &= \sum_{i=1}^{I} \alpha_i \exp\left(-j2\pi \boldsymbol{f} \tau_i^l\right) + \boldsymbol{n}_l \end{aligned} \quad (24)$$

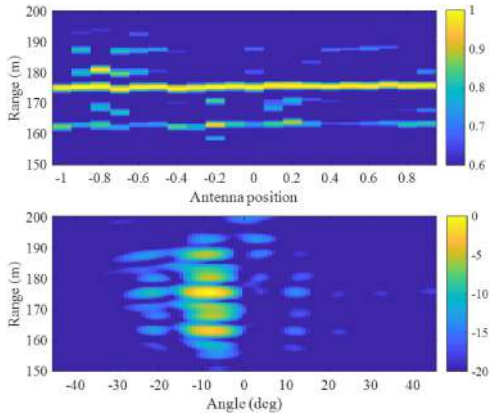

Fig. 22. Range profiles (top) and 2-D focused image (bottom) of the high building with a dynamic range of 20 dB.

where τ_i^l denotes the time delay between the ith target and the lth antenna position. Then, the range compression can be conducted by applying Fourier transform, giving $\boldsymbol{\chi}_l{}' = \boldsymbol{\Phi}^H \boldsymbol{s}_l{}'(\boldsymbol{f})$. Finally, azimuth compression can be obtained by applying BP algorithm, giving

$$\widetilde{\alpha}(r,\theta) = \sum_{l=1}^{L} \boldsymbol{\chi}_l{}' \left(2\sqrt{(x_l - r\sin\theta)^2 + (r\cos\theta)^2}/c \right) \quad (25)$$

where $\widetilde{\alpha}(r,\theta)$ is the estimated amplitude of the point at (r,θ) and $\boldsymbol{\chi}_l{}'(2\sqrt{(x_l - r\sin\theta)^2 + (r\cos\theta)^2}/c)$ is calculated by the linear interpolation process.

However, similar with the previous time delay estimation case, directly conducting range compression with gapped frequencies will cause high-level artifacts in the range direction, and thus in the focused image, as shown in Fig. 22. One solution is to use the previously proposed MC-based method to recover the missing frequency components. However, it should be noticed that, in such a case, the matrix reconstruction needs to be performed at each antenna position separately, which is time consuming, and the low-rank property may not be well satisfied when more targets are imaged because of the limited signal matrix size. In the following, another MC-based method is formulated to simultaneously recover the gapped frequency components for all antenna positions.

When $r_i > 2(L_0)^2/\lambda$ (in our case, the target is at about 175 m, the aperture length L_0 is 2 m, and the wavelength λ is about 61 cm, therefore, this condition is well satisfied), the time delay of the ith target at (r_i, θ_i) can be approximated by $\tau_i^l \simeq 2(r_i - x_l \sin\theta_i)/c$, resulting in

$$\begin{aligned} &\boldsymbol{S}(o,l) \\ &\simeq \sum_{i=1}^{I} \alpha_i \mathrm{e}^{-j2k_o r_i} \mathrm{e}^{j4\pi x_l \sin\theta_i/\lambda} \mathrm{e}^{j4\pi(o-O/2)\Delta f x_l \sin\theta_i/c} \\ &\quad + \boldsymbol{N}(o,l) \end{aligned} \quad (26)$$

where $\boldsymbol{S}$ is the received signal matrix, and $k_o = 2\pi f_o/c$ is the oth wavenumber ($o = 1, 2, \ldots, O$). According to [51], if $4\pi(o - O/2)\Delta f x_l \sin\theta_i/c \le \pi/2$, the third exponential term of (26) can be discarded. To satisfy this condition, we can assume the following equation to be satisfied:

$$\begin{aligned} &\max\{4\pi(o - O/2)\Delta f x_l \sin\theta_i/c\} \\ &\quad = 4\pi \frac{B}{2}\frac{L_0}{2c} = \frac{\pi}{2}\frac{L_0}{c/2B} \le \frac{\pi}{2} \Rightarrow \frac{L_0}{\Delta r_{\max}} \le 1. \end{aligned} \quad (27)$$

Since the maximal range resolution $\Delta r_{\max}$ is 3.57 m and the aperture length L_0 is 2 m, condition (27) can be satisfied. Therefore, the third exponential term of the right-hand side of (26) is discarded in the following, giving the signal matrix as

$$\boldsymbol{S}_{O\times L} \simeq \boldsymbol{A}_{O\times I} \boldsymbol{\Lambda}_{I\times I} \boldsymbol{B}^T_{L\times I} + \boldsymbol{N}_{O\times L} \quad (28)$$

where $\boldsymbol{A} = [\boldsymbol{a}_1, \ldots, \boldsymbol{a}_I]$ with $\boldsymbol{a}_i = [e^{-j2k_1 r_i}, \ldots, e^{-j2k_O r_i}]^T$, $\boldsymbol{B} = [\boldsymbol{b}_1, \ldots, \boldsymbol{b}_I]$ with $\boldsymbol{b}_i = [\mathrm{e}^{j4\pi x_1 \sin\theta_i/\lambda}, \ldots, \mathrm{e}^{j4\pi x_L \sin\theta_i/\lambda}]^T$, $\boldsymbol{\Lambda} = \mathrm{diag}\{[\alpha_1, \ldots, \alpha_I]\}$, and thus the rank of $\boldsymbol{S}$ is bounded by $\mathrm{rank}(\boldsymbol{S}) \le \mathrm{rank}(\boldsymbol{\Lambda}_{I\times I}) = I$.

Then, the received signal matrix $\boldsymbol{S}$ can be rearranged as a matrix $\boldsymbol{S}_{\mathrm{st}}^0$ with a two-fold Hankel structure [49], [50]. According to the structured MC theory, $\mathrm{rank}(\boldsymbol{S}_{\mathrm{st}}^0) \le \mathrm{rank}(\boldsymbol{\Lambda}_{I\times I}) = I$. In such a case, the rank of $\boldsymbol{S}_{\mathrm{st}}^0$ is still bounded by the number of targets, and the full columns/rows missing problem of $\boldsymbol{S}$ disappears. Therefore, the gapped frequency components can be estimated by solving the following optimization problem:

$$\min \|\boldsymbol{S}_{\mathrm{st}}\|_* \quad \text{s.t.} \left\| P_{\Omega}^{\mathrm{st}}(\boldsymbol{S}_{\mathrm{st}} - \boldsymbol{S}_{\mathrm{st}}^0) \right\|_F \le \varepsilon_{\mathrm{st}}. \quad (29)$$

At last, rearranging the estimated structured matrix $\boldsymbol{S}_{st}$ to its original form, we can get the spectral gap filled signal matrix $\boldsymbol{S}_{\mathrm{MC}}$, with which the focused SAR image can be obtain by 2-D Fourier transform.

$$\widetilde{\boldsymbol{\Lambda}}_{\mathrm{MC}} = \boldsymbol{\Phi}_1^H \boldsymbol{S}_{\mathrm{MC}} \boldsymbol{\Phi}_2^* \quad (30)$$

where $\boldsymbol{\Phi}_1$ is the Fourier transform matrix in range direction and $\boldsymbol{\Phi}_2$ is the inverse Fourier transform matrix in azimuth direction. According to the method presented above, SAR image of the building is obtained as shown in the top of Fig. 23 with a dynamic range of 20 dB. After filling the frequency gaps by the proposed method, we can effectively suppress the high-level artifacts and improve the imaging quality compared with Fig. 22, which is

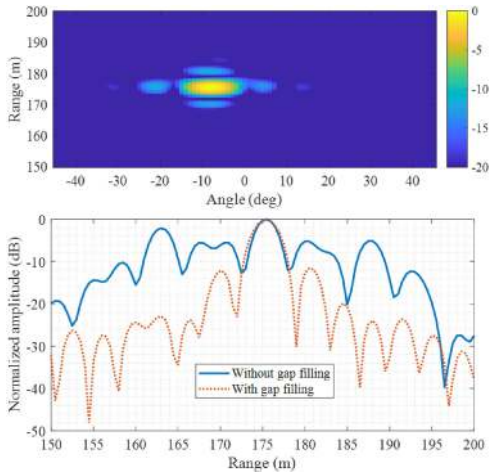

Fig. 23. Top: 2-D focused image of the high building obtained by the proposed spectral gap filling method. Bottom: Comparison between Figs. 22 and 23 in the range direction at $-9°$.

further validated in the bottom of Fig. 23. We note that, for the result obtained by the proposed method, the main lobe is slightly wider than that without gap filling. This is caused by the intrinsic Fourier transform property of the frequency gapped signal, not by the proposed method.

Furthermore, compressive-sensing-based gap filling method is used to obtain the focused SAR image of the building for comparison purpose. First, based on (28), the received signal corresponding to the useful frequency bands can be written as

$$\boldsymbol{S}^0 = \boldsymbol{\Theta}\boldsymbol{S} \simeq (\boldsymbol{\Theta}\boldsymbol{A})\boldsymbol{\Lambda}_{I\times I}\boldsymbol{B}^T + \boldsymbol{N}^0 \tag{31}$$

where $\boldsymbol{\Theta} \in R^{NM\times O}$ with $NM < O$ is the measurement matrix corresponding to the useful frequency bands (there are totally N useful bands and each band has M frequencies). Then, two sparsifying dictionaries $\boldsymbol{\Psi}_1$ and $\boldsymbol{\Psi}_2$ in range direction and azimuth direction can be designed to express the signal $\boldsymbol{S}^0$ as

$$\boldsymbol{S^0} = (\boldsymbol{\Theta}\boldsymbol{\Psi}_1)\boldsymbol{\Lambda}^0_{\text{CS}}\boldsymbol{\Psi}_2^T + \boldsymbol{N}^0 \tag{32}$$

where $\boldsymbol{\Psi}_1$ and $\boldsymbol{\Psi}_2$ are complete or overcomplete discrete Fourier transform matrices designed by discretizing the range and angle domain. If $\boldsymbol{\Lambda}^0_{\text{CS}}$ is sparse, it can be estimated by

$$\begin{aligned} &\widetilde{\boldsymbol{\Lambda}}^0_{\text{CS}} = \min \left\|\boldsymbol{\Lambda}^0_{\text{CS}}\right\|_0 \\ &\text{s.t.} \left\|\boldsymbol{S}^0 - (\boldsymbol{\Theta}\boldsymbol{\Psi}_1)\boldsymbol{\Lambda}^0_{\text{CS}}\boldsymbol{\Psi}_2^T\right\|_F \le \varepsilon_{\text{noise}} \end{aligned} \tag{33}$$

which can be solved by 2-D OMP algorithm [52] or 2-D SL0 algorithm [53]. According to [29], to compare the compressive-sensing-based method with the conventional method, $\widetilde{\boldsymbol{\Lambda}}^0_{\text{CS}}$ is used to obtain the gap-filled signal as $\boldsymbol{S}_{\text{CS}} = \boldsymbol{\Psi}_1\widetilde{\boldsymbol{\Lambda}}^0_{\text{CS}}\boldsymbol{\Psi}_2^T$. Finally, similar to (30), the focused SAR image is achieved by

$$\widetilde{\boldsymbol{\Lambda}}_{\text{CS}} = \boldsymbol{\Phi}_1^H\boldsymbol{S}_{\text{CS}}\boldsymbol{\Phi}_2^*. \tag{34}$$

When a Fourier transform dictionary is used, which is just the case considered in this paper, sparse recovery algorithms that rely on the accuracy of best k-term approximations for their performance guarantees, such as the basis pursuit algorithm and the greedy algorithms (e.g., OMP algorithm), may experience performance degradation due to the offgrid problem caused by the discretization, as shown in [31]. Specifically, in reality, the target cannot be exactly located at the defined range-angle grid (the so-called offgrid problem), resulting in estimation errors in solving (33). As a consequence, the performance of compressive-sensing-based gap filling method will be degraded.

In the following, 2-D OMP algorithm is used to solve (33) for its efficiency, where the dictionary $\boldsymbol{\Psi}_1$ is a complete Fourier transform matrix (with range interval same as the system range resolution) and dictionary $\boldsymbol{\Psi}_2$ is an overcomplete Fourier transform matrix (with angle interval equaling to 2°), giving the result shown in the top of Fig. 24. A comparison is performed with the result obtained by decreasing the cell size in dictionary $\boldsymbol{\Psi}_1$ to 20 times smaller than the system range resolution, which is shown in the middle of Fig. 24. Their comparison in range direction at -9° is shown in the bottom of Fig. 24. It can be seen that, with a complete range dictionary, the estimated target range is not exactly consistent with the result obtained without filling frequency gaps, which demonstrates the influence of offgrid problem. By using an overcomplete range dictionary, the

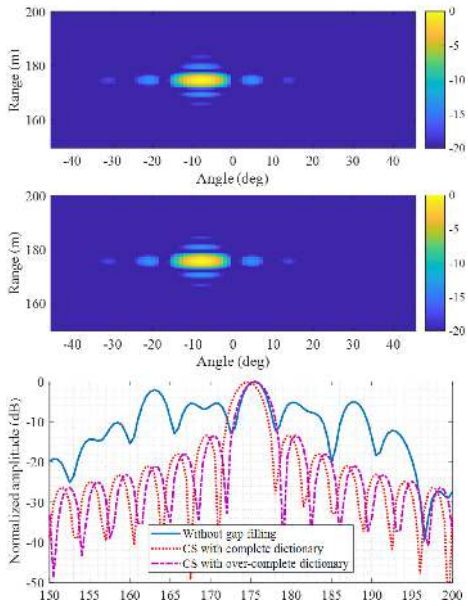

Fig. 24. 2-D focused image of the high building obtained by compressive-sensing-based method with (Top) a complete range dictionary and (Middle) an overcomplete range dictionary. Bottom: Comparison in the range direction.

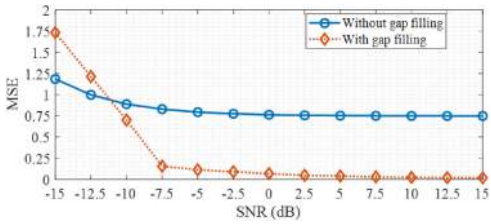

Fig. 25. MSEs against different SNR levels.

estimated target range becomes more accurate. Therefore, it can be learned that, when using compressive-sensing-based gaps filling method, extra attention may be needed to account for the effects of offgrid problem of the designed dictionaries. On the contrary, for the proposed MC-based method, no sparsifying dictionary is required, which is its advantage.

At last, simulations have been conducted to evaluate the proposed MC-based frequency gap filling method with different SNR conditions, different target numbers, and different useful frequency bands. The simulation parameters are almost same as that used in high building SAR imaging experiment, except the integration time is changed to 4 μs to reduce the running time, and the mean square error (MSE), defined as

$$\text{MSE} = ||\widetilde{\boldsymbol{\Lambda}}_{\text{MC}} - \boldsymbol{\Lambda}_{\text{ref}}||_F / ||\boldsymbol{\Lambda}_{\text{ref}}||_F \tag{35}$$

is used as the evaluation index of the image quality, where $\boldsymbol{\Lambda}_{\text{ref}}$ is the reference SAR image obtained without frequency gaps or additive white Gaussian noise. For each condition, simulations were repeated 50 times and the MSEs were averaged. First, similar to the high building imaging case, a target located at (175 m, 0°) is considered with different SNR levels (from -15 to 15 dB with a 2.5 dB step). The MSEs against different SNRs of the SAR images obtained with and without filling frequency gaps are shown in Fig. 25. It can be seen that, when the SNR is higher than -10 dB, by filling gaps and denoising, the proposed

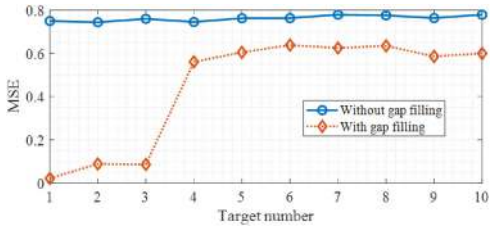

Fig. 26. MSEs against different target numbers.

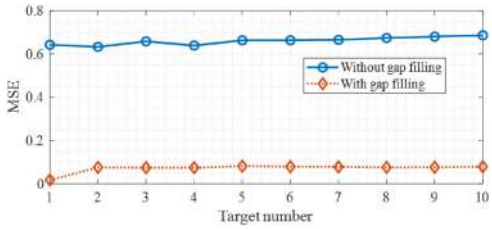

Fig. 27. MSEs against different target numbers with one additional channel.

method can perform well and achieve smaller MSEs than the results obtained with frequency gaps, especially after SNR becomes higher than -7.5 dB (where the MSEs with and without gaps filling are 0.156 and 0.830, respectively).

Second, the proposed method is evaluated with different numbers of targets (from 1 to 10). The obtained MSEs against target numbers are shown in Fig. 26, where the SNR is set to be 10 dB. Although better than the result without gap filling, the performance of the proposed method degrades drastically when there are more than three targets. It occurs because the frequency gaps are not randomly distributed but located at fixed positions; although the two-fold Hankel structure can reduce the influence of full rows/columns missing problem, the missing entries in the signal matrix $\boldsymbol{S}_{\text{st}}^0$ are not randomly distributed. Therefore, the performance of the proposed method will be degraded when the target number is increased, as indicated by [50].

Third, to show the effect of available frequency bands on the proposed method, one more channel is added, whose central frequency is 485 MHz (previously, we were using three channels with central frequencies 473, 497, and 509 MHz). After adding this channel, the gapped bandwidth between two adjacent channels becomes uniform and equivalent to the bandwidth of one TV channel. In such a case, the obtained MSE as a function of target number is shown in Fig. 27, where the SNR is also 10 dB. Compared to Fig. 26, the proposed method always perform well and almost does not degrade with the increase of the target number up to 10. This is because, when four channels are available, although missing entries in the signal matrix $\boldsymbol{S}_{\text{st}}^0$ are still not randomly distributed, the number of missing entries is reduced, which can help to result in a better performance.

To summarize, the proposed MC-based frequency gap filling method can perform well in noisy conditions, especially when SNR is higher than -7.5 dB. Although still works, the performance of the proposed method may be degraded when there are large number of targets in the imaged scene. Its performance can be further improved by reducing the number of missing entries, i.e., by employing more channels.

V. Conclusion

A PBR system using ISDB-T/S digital TV signal with COTS hardware is presented in this paper. The imaging capability of this system is validated by various experiments with far-range and short-range targets. Some practical issues of using ISDB-T/S as illuminating sources for PBR application are highlighted. Inverse filter is proved to be effective to reduce the influence of signal structure on the range compression result, and frequency drift correction of different LNBs can help to increase the SNR. Multiple ISDB-T/S channels can be combined to increase the range resolution, while the high-level artifacts caused by the spectral gaps should be well suppressed. Super-SVA-based method and two low-rank MC-based methods are proposed to do so, which are validated to be effective by 1-D time delay estimation experiments, 2-D stationary target imaging experiments, and some evaluation simulations. The proposed methods can also be used for other passive radar imaging applications with different digital TV standards, such as DVB-T/S and DMTB. For ISDB-S-based 2-D imaging, synthetic aperture processing in azimuth direction cannot be conducted currently due to the nonsynchronized initial phases, which is one of the next research steps. Another consideration is to increase the observation range by replacing current surveillance antennas with dedicated antennas and changing the data acquisition interface and platform. Polarization information might also be exploited for a better understanding of the imaged targets.

References

[1] L. Daniel, S. Hristov, X. Lyu, A. G. Stove, M. Cherniakov, and M. Gashinova, "Design and validation of a passive radar concept for ship detection using communication satellite signals," *IEEE Trans. Aerosp. Electron. Syst.*, vol. 53, no. 6, pp. 3115–3134, Dec. 2017.

[2] H. D. Griffiths and C. J. Baker, *An Introduction to Passive Radar*. Norwood, MA, USA: Artech House, 2017.

[3] M. Antoniou and M. Cherniakov, "GNSS-based bistatic SAR: A signal processing view," *EURASIP J. Adv. Signal Process.*, vol. 2013, no. 1, 2013, Art. no. 98.

[4] L. Lestarquit *et al.*, "Reflectometry with an open-source software GNSS receiver: Use case with carrier phase altimetry," *IEEE J. Sel. Topics Appl. Earth Observ. Remote Sens.*, vol. 9, no. 10, pp. 4843–4853, Oct. 2016.

[5] D. Gromek, K. Kulpa, and P. Samczyński, "Experimental results of passive SAR imaging using DVB-T illuminators of opportunity," *IEEE Geosci. Remote Sens. Lett.*, vol. 13, no. 8, pp. 1124–1128, Aug. 2016.

[6] M. Martorella and E. Giusti, "Theoretical foundation of passive bistatic ISAR imaging," *IEEE Trans. Aerosp. Electron. Syst.*, vol. 50, no. 3, pp. 1647–1659, Jul. 2014.

[7] K. Chetty, G. E. Smith, and K. Woodbridge, "Through-the-wall sensing of personnel using passive bistatic WiFi radar at standoff distances," *IEEE Trans. Geosci. Remote Sens.*, vol. 50, no. 4, pp. 1218–1226, Apr. 2012.

[8] P. Marques, A. Ferreira, F. Fortes, P. Sampaio, H. Rebelo, and L. Reis, "A pedagogical passive radar using DVB-S signals," in *Proc. 3rd IEEE Int. Asia-Pacific Conf. Synthetic Aperture Radar*, 2011, pp. 1–4.

[9] F. Liu, M. Antoniou, Z. Zeng, and M. Cherniakov, "Coherent change detection using passive GNSS-based BSAR: Experimental proof of concept," *IEEE Trans. Geosci. Remote Sens.*, vol. 51, no. 8, pp. 4544–4555, Aug. 2013.

[10] F. Liu, X. Fan, T. Zhang, and Q. Liu, "GNSS-based SAR interferometry for 3-D deformation retrieval: Algorithms and feasibility study," *IEEE Trans. Geosci. Remote Sens.*, vol. 56, no. 10, pp. 5736–5748, Oct. 2018.

[11] J. Shi, Y. Liu, W. Liu, and X. Zhang, "High-resolution synthetic aperture radar based on the IEEE 802.11 protocol," *Electron. Lett.*, vol. 51, no. 22, pp. 1815–1817, 2015.

[12] W. Feng, J.-M. Friedt, Z. Hu, G. Cherniak, and M. Sato, "WiFi-based imaging for GPR applications: Fundamental study and experimental results," in *Proc. IET Int. Radar Conf.*, 2018, pp. 1–5.

[13] L. M. Ulander, P.-O. Frölind, A. Gustavsson, R. Ragnarsson, and G. Stenström, "Airborne passive SAR imaging based on DVB-T signals," in *Proc. IEEE Int. Conf. Geosci. Remote Sens. Symp.*, 2017, pp. 2408–2411.

[14] A. Capria *et al.*, "Ship detection with DVB-T software defined passive radar," in *Proc. IEEE Gold Remote Sens. Conf.*, vol. 1, Apr. 2010, pp. 3–5.

[15] M. Baczyk, P. Samczynski, and K. Kulpa, "Passive ISAR imaging of air targets using DVB-T signals," in *Proc. IEEE Radar Conf.*, 2014, pp. 0502–0506.

[16] S. Brisken, M. Moscadelli, V. Seidel, and C. Schwark, "Passive radar imaging using DVB-S2," in *Proc. Radar Conf.*, 2017, pp. 0552–0556.

[17] M. Conti, C. Moscardini, and A. Capria, "Dual-polarization DVB-T passive radar: Experimental results," in *Proc. Radar Conf.*, 2016, pp. 1–5.

[18] J. E. Palmer, H. A. Harms, S. J. Searle, and L. M. Davis, "DVB-T passive radar signal processing," *IEEE Trans. Signal Process.*, vol. 61, no. 8, pp. 2116–2126, Apr. 2013.

[19] K. Polonen and V. Koivunen, "Detection of DVB-T2 control symbols in passive radar systems," in *Proc. Sensor Array Multichannel Signal Process. Workshop*, 2012, pp. 309–312.

[20] S. Nakamura *et al.*, "An experimental study of enhancement of the cross-range resolution of ISAR imaging using ISDB-T digital TV based passive bistatic radar," in *Proc. Geosci. Remote Sens. Symp.*, 2011, pp. 2837–2840.

[21] X. Wan, J. Wang, H. Sheng, and T. Hui, "Reconstruction of reference signal for DTMB-based passive radar systems," in *Proc. IEEE CIE Int. Conf. Radar*, 2011, pp. 165–168.

[22] W. Feng, J.-M. Friedt, G. Cherniak, and M. Sato, "Passive bistatic radar moving target detection using software defined radio," *Rev. Sci. Instrum.*, vol. 88, no. 10, 2018, Art. no. 104701.

[23] Z. Sun, T. Wang, T. Jiang, C. Chen, and W. Chen, "Analysis of the properties of DVB-S signal for passive radar application," in *Proc. Int. Conf. Wireless Commun. Signal Process.*, 2013, pp. 1–5.

[24] H. Asami and M. Sasaki, "Outline of ISDB systems," *Proc. IEEE*, vol. 94, no. 1, pp. 248–250, Jan. 2006.

[25] J. Honda and T. Otsuyama, "Feasibility study on aircraft positioning by using ISDB-T signal delay," *IEEE Antennas Wireless Propag. Lett.*, vol. 15, pp. 1787–1790, Mar. 2016, doi: 10.1109/LAWP.2016.2536725.

[26] W. Feng, J. Friedt, G. Cherniak, and M. Sato, "Novel algorithm for high resolution passive radar imaging with ISDB-T digital TV signal," in *Proc. IEEE Int. Geosci. Remote Sens. Symp.*, Valencia, Spain, Jul. 2018, pp. 6687–6690.

[27] H. Ma, M. Antoniou, and M. Cherniakov, "Passive GNSS-based SAR resolution improvement using joint galileo E5 signals," *IEEE Geosci. Remote Sens. Lett.*, vol. 12, no. 8, pp. 1640–1644, Aug. 2015.

[28] D. Olivadese, E. Giusti, D. Petri, M. Martorella, A. Capria, and F. Berizzi, "Passive ISAR with DVB-T signals," *IEEE Trans. Geosci. Remote Sens.*, vol. 51, no. 8, pp. 4508–4517, Aug. 2013.

[29] W. Qiu *et al.*, "Compressive sensing-based algorithm for passive bistatic ISAR with DVB-T signals," *IEEE Trans. Aerosp. Electron. Syst.*, vol. 51, no. 3, pp. 2166–2180, Jul. 2015.

[30] Y. Zheng, Y. Yang, and W. Chen, "A novel range compression algorithm for resolution enhancement in GNSS-SARS," *Sensors*, vol. 17, no. 7, 2017, Art. no. 1496.

[31] Y. Chi, L. L. Scharf, A. Pezeshki, and A. R. Calderbank, "Sensitivity to basis mismatch in compressed sensing," *IEEE Trans. Signal Process.*, vol. 59, no. 5, pp. 2182–2195, May 2011.

[32] O. Teke, A. C. Gurbuz, and O. Arikan, "Perturbed orthogonal matching pursuit," *IEEE Trans. Signal Process.*, vol. 61, no. 24, pp. 6220–6231, Dec. 2013.

[33] E. J. Candès and B. Recht, "Exact matrix completion via convex optimization," *Found. Comput. Math.*, vol. 9, no. 6, 2009, Art. no. 717.

[34] E. J. Candes and Y. Plan, "Matrix completion with noise," *Proc. IEEE*, vol. 98, no. 6, pp. 925–936, Jun. 2010.

[35] M. A. Davenport and J. Romberg, "An overview of low-rank matrix recovery from incomplete observations," *IEEE J. Sel. Topics Signal Process.*, vol. 10, no. 4, pp. 608–622, Jun. 2016.

[36] M. Takada and M. Saito, "Transmission system for ISDB-T," *Proc. IEEE*, vol. 94, no. 1, pp. 251–256, Jan. 2006.

[37] H. Katoh, "Transmission system for ISDB-S," *Proc. IEEE*, vol. 94, no. 1, pp. 289–295, Jan. 2006.

[38] J. Salzman, D. Akamine, R. Lefevre, and J. C. Kirk, "Interrupted synthetic aperture radar (SAR)," *IEEE Aerosp. Electron. Syst. Mag.*, vol. 17, no. 5, pp. 33–39, May 2002.

[39] H. Stankwitz and M. Kosek, "Sparse aperture fill for SAR using Super-SVA," in *Proc. IEEE Nat. Radar Conf.*, 1996, pp. 70–75.

[40] L. Zhuang, X. Liu, and Z. Zhou, "Enhanced resolution for sparse aperture radar imaging using Super-SVA," in *Proc. Asia-Pacific Microw. Conf.*, 2008, pp. 1–4.

[41] D. Olivadese, M. Martorella, and F. Berizzi, "Multi-channel P-ISAR grating lobes cancellation," in *Proc. IET Int. Conf. Radar Syst.*, 2013, pp. 1–5.

[42] H. C. Stankwitz, R. J. Dallaire, and J. R. Fienup, "Spatially variant apodization for sidelobe control in SAR imagery," in *Proc. IEEE Nat. Radar Conf.*, 1994, pp. 132–137.

[43] W. Feng, L. Yi, and M. Sato, "Near range radar imaging based on block sparsity and cross-correlation fusion algorithm," *IEEE J. Sel. Topics Appl. Earth Observ. Remote Sens.*, vol. 11, no. 6, pp. 2079–2089, Jun. 2018.

[44] Z. Ding, W. Yin, T. Zeng, and T. Long, "Radar parameter design for geosynchronous SAR in squint mode and elliptical orbit," *IEEE J. Sel. Topics Appl. Earth Observ. Remote Sens.*, vol. 9, no. 6, pp. 2720–2732, Jun. 2016.

[45] Z. Lin, M. Chen, and Y. Ma, "The augmented lagrange multiplier method for exact recovery of corrupted low-rank matrices," 2010, arXiv:1009.5055.

[46] X. Hu, N. Tong, S. Ding, X. He, and X. Zhao, "ISAR imaging with sparse stepped frequency waveforms via matrix completion," *Remote Sens. Lett.*, vol. 7, no. 9, pp. 847–854, 2016.

[47] H. Bi, C. Jiang, B. Zhang, Z. Wang, and W. Hong, "Radar change imaging with undersampled data based on matrix completion and Bayesian compressive sensing," *IEEE Geosci. Remote Sens. Lett.*, vol. 12, no. 7, pp. 1546–1550, Jul. 2015.

[48] H. Bi, B. Zhang, W. Hong, and S. Zhou, "Matrix-completion-based airborne tomographic SAR inversion under missing data," *IEEE Geosci. Remote Sens. Lett.*, vol. 12, no. 11, pp. 2346–2350, Nov. 2015.

[49] Y. Chen and Y. Chi, "Spectral compressed sensing via structured matrix completion," *IEEE Trans. Inf. Theory*, vol. 60, no. 10, pp. 6576–6601, Oct. 2014.

[50] X. Hu, N. Tong, J. Wang, S. Ding, and X. Zhao, "Matrix completion-based MIMO radar imaging with sparse planar array," *Signal Process.*, vol. 131, pp. 49–57, 2017.

[51] J. Fortuny-Guasch, "A fast and accurate far-field pseudopolar format radar imaging algorithm," *IEEE Trans. Geosci. Remote Sens.*, vol. 47, no. 4, pp. 1187–1196, Apr. 2009.

[52] Y. Fang, J. Wu, and B. Huang, "2D sparse signal recovery via 2D orthogonal matching pursuit," *Sci. China Inf. Sci.*, vol. 55, no. 4, pp. 889–897, 2012.

[53] A. Ghaffari, M. Babaie-Zadeh, and C. Jutten, "Sparse decomposition of two dimensional signals," in *Proc. IEEE Int. Conf. Acoust., Speech Signal Process.*, 2009, pp. 3157–3160.